Xiuying Wang
College of Mechanical Electrical Engineering,
Nanjing University of Aeronautics
and Astronautics,
Nanjing 210016, China
e-mail: wangxy621@163.com

Liping Shi
College of Mechanical Electrical Engineering,
Nanjing University of Aeronautics and
Astronautics,
Nanjing 210016, China;
School of Mechanical Engineering,
Anhui University of Technology,
Ma'anshan 243000, China
e-mail: xiaopingguoshi@163.com

Wei Huang
College of Mechanical Electrical Engineering,
Nanjing University of Aeronautics
and Astronautics,
Nanjing 210016, China
e-mail: huangwei@nuaa.edu.cn

Xiaolei Wang[1]
College of Mechanical Electrical Engineering,
Nanjing University of Aeronautics
and Astronautics,
Nanjing 210016, China
e-mail: wxl@nuaa.edu.cn

A Multi-Objective Optimization Approach on Spiral Grooves for Gas Mechanical Seals

Spiral groove is one of the most common types of structures on gas mechanical seals. Numerical research demonstrated that the grooves designed for improving gas film lift or film stiffness often lead to the leakage increase. Hence, a multi-objective optimization approach specially for conflicting objectives is utilized to optimize the spiral grooves for a specific sample in this study. First, the objectives and independent variables in multi-objective optimization are determined by single objective analysis. Then, a set of optimal parameters, i.e., Pareto-optimal set, is obtained. Each solution in this set can get the highest dimensionless gas film lift under a specific requirement of the dimensionless leakage rate. Finally, the collinearity diagnostics is performed to evaluate the importance of different independent variables in the optimization. [DOI: 10.1115/1.4038864]

Keywords: spiral grooves, structures, multi-objective optimization, mechanical seals

1 Introduction

Wear and leakage increase dramatically when the mechanical seals run under severe conditions. Enhancing the performance of mechanical seals is of great significance to high durability and reliability of modern machines. The approach of designing specific structures on the friction surface is becoming a research hotspot in the field of interface science since it has been proven to be an effective means to improve the interfacial properties [1–6].

Many studies have been conducted to improve the load carrying characteristic or friction property by processing structures such as microdimples, microgrooves, and spiral grooves on mechanical seals [1–17]. The benefits mainly include increasing load carrying capacity [1,7–12] and fluid film stiffness [1], reducing friction [8,10–13] and wear [1,10,13,14]. Among them, spiral groove is a mainstream structure type and is extensively employed in dry gas seal and upstream pumping seal to improve their performances under complex situations. Different from the ordinary friction pairs, the leakage property is a critical factor for mechanical seals. In order to obtain a low leakage rate, friction, and wear, various studies have been performed to optimize the geometrical parameters of spiral grooves. However, many studies found that the leakage also tends to increase, while the gas film lift or film stiffness is improved by spiral grooves [18–22]. For instance, it is found that the film pressure and leakage both increase because of the microscale effects of spiral grooves [20], the opening force and leakage rate show a similar variation with the speed number [21] and the spiral groove parameters [22]. It means that the leakage property and the load carrying characteristic or friction property are conflicting in many cases. In view of this, these properties need to be considered synthetically in the parameters optimization of spiral grooves.

Nevertheless, most studies analyzed these objectives using single objective analysis rather than multi-objective analysis. For instance, only the bearing force was regarded as the design objective for the optimization of spiral groove while the leakage rate was regarded as a constraint condition [23], and the load carrying capacity and leakage rate were investigated under different parameters of surface textures, respectively [19]. The optimal parameters of spiral grooves obtained by a single objective optimization are often affected by researcher's subjective judgments. It is difficult to obtain a better combination performance of mechanical seals objectively due to the conflict between leakage property and load carrying characteristic or friction property.

Multi-objective optimization approach is a method specially for conflicting objectives. Certainly, there are a few studies involving multiple objectives. Liu et al. [24] established a multi-objective model including fluid film axial stiffness and flow leakage, which promotes the optimization of spiral grooves on mechanical seals greatly. Nevertheless, the results given in the study are still the variations of each objective with different spiral groove parameters, respectively.

Therefore, a multi-objective optimization approach is presented in this study, and then a sample that is optimizing the spiral grooves on gas mechanical seals under a specific condition is solved using this approach. In order to determine the important parameters of spiral grooves and the main performance parameters reasonably in the multi-objective optimization, the influences of spiral groove parameters on the dimensionless gas film lift, dimensionless axial gas film stiffness, coefficient of friction (COF), and dimensionless leakage rate are first analyzed, respectively. Then, the model of multi-objective optimization is established, and the Pareto-optimal set is obtained. Each solution in this set can get the highest dimensionless gas film lift under a specific requirement of the dimensionless leakage rate. Finally, collinearity diagnostics is

[1]Corresponding author.

Contributed by the Tribology Division of ASME for publication in the JOURNAL OF TRIBOLOGY. Manuscript received July 3, 2017; final manuscript received December 24, 2017; published online January 31, 2018. Assoc. Editor: Stephen Boedo.

performed to evaluate the importance of different parameters in the optimization results.

2 Analytical Model

2.1 Physical Model and Design Variables. Figure 1 shows the schematic diagram of mechanical seals by two mating rings and the geometrical model of the grooved ring. Spiral grooves are uniformly distributed in the circumferential direction on the rotating seal. The stationary ring is smooth. Whereby r_i and r_o represent the inner and outer radii of the rings, respectively; the sealing faces are separated by a layer of gas film, i.e., the sealing clearance h_0; U is the angular velocity; r_g is the radius of spiral groove roots; h_g is the groove depth, and n is the number of grooves. The type of spiral is logarithmic, and its equation is expressed as

$$r = r_i e^{\theta \tan \beta} \tag{1}$$

where r and θ are the polar coordinates in the radial and circumferential directions, respectively, and e is the natural constant. The investigated spiral groove parameters include spiral angle β, groove-dam ratio δ, groove-land ratio κ, and ratio of groove depth and film thickness χ. The definitions of δ, κ, and χ are presented as

$$\delta = \frac{r_o - r_g}{r_o - r_i}, \quad \kappa = \frac{\alpha}{\varphi}, \quad \chi = \frac{h_g}{h_0} \tag{2}$$

In order to ensure the accuracy of the computed results, the entire rotating seal face is selected as the calculation domain.

2.2 Governing Equations and Objective Functions. The steady-state Reynolds equation in polar coordinates is employed to analyze the gas film pressure distribution. Due to the compressibility of gas which is significantly higher than that of fluid, the density of gas is considered in the governing equation expressed as

$$\frac{\partial}{\partial r}\left(\frac{\rho r h^3}{\mu}\frac{\partial p}{\partial r}\right) + \frac{1}{r}\frac{\partial}{\partial \theta}\left(\frac{\rho h^3}{\mu}\frac{\partial p}{\partial \theta}\right) = 6Ur\frac{\partial(\rho h)}{\partial \theta} \tag{3}$$

where μ is the dynamic viscosity of gas, ρ is the gas density, p is the gas pressure, and h is the gas film thickness which can be expressed as

$$h(r,\theta) = \begin{cases} h_0 + h_g & (r,\theta) \in \text{groove region} \\ h_0 & (r,\theta) \notin \text{groove region} \end{cases} \tag{4}$$

Assuming that the sealing gas is ideal, viscous and has a constant dynamic viscosity μ. In addition, the gas can be assumed as an isothermal flow because the COF of noncontact gas film seals is very small and the temperature rises slowly. The ideal gas state equation is written as

$$\frac{p}{\rho} = \frac{RT}{M} = \gamma \tag{5}$$

where M is the average molecular mass of gas which is equal to 29 g/mol; R is the proportional constant of the ideal gas, equal to 8.314 cm^3 MPa/mol K; and T is the absolute temperature of sealing system and is taken as 300 K. Substituting Eq. (5) into Eq. (3), the Reynolds equation can be written as

$$\frac{\partial}{\partial r}\left(\frac{prh^3}{\mu}\frac{\partial p}{\partial r}\right) + \frac{1}{r}\frac{\partial}{\partial \theta}\left(\frac{ph^3}{\mu}\frac{\partial p}{\partial \theta}\right) = 6Ur\frac{\partial ph}{\partial \theta} \tag{6}$$

The boundary pressures at the inner radius and the outer radius of seals are p_i and p_o, respectively. Mandatory boundary conditions are applied for $\theta = 0$ and $\theta = 2\pi$ because they are actually the same border but are treated as two borders in the calculation. The boundary conditions of calculation domain are expressed as

$$\begin{cases} p(r = r_i, \theta) = p_i \\ p(r = r_o, \theta) = p_o \\ p(r, \theta = 0) = p(r, \theta = 2\pi) \\ \dfrac{\partial p}{\partial \theta}(r, \theta = 0) = \dfrac{\partial p}{\partial \theta}(r, \theta = 2\pi) \end{cases} \tag{7}$$

The gas film lift W is the integral of the gas film pressure across the entire seal face. The leakage rate Q is the flow rate in the radial direction and it should follow the flow continuity principle. It could be calculated no matter which radius is chosen. In fact, it was checked at several radii and the results were very close within the allowable range of the error. So, the inner radius is adopted in the following evaluation. The COF is generated mainly by shearing force inside the fluid film for noncontact seals. Asperity contact may appear at the start or stop or unstable operation, which can be ignored for the simplification. The performance parameters are expressed as

$$\text{gas film lift}: W = \int_0^{2\pi}\int_{r_i}^{r_o} p(r,\theta) r dr d\theta \tag{8}$$

$$\text{coefficient of friction}: \text{COF} = \int_0^{2\pi}\int_{r_i}^{r_o}\left(\frac{\partial p}{r\partial \theta} \times \frac{h}{2} + \mu\frac{Ur}{h}\right) r dr d\theta / W \tag{9}$$

$$\text{leakage rate}: Q = -\int_0^{2\pi}\left(\frac{prh^3}{12\mu\gamma}\frac{\partial p}{\partial r}\right)_{r=r_i} d\theta \tag{10}$$

Axial gas film stiffness K is one of the important parameters to describe the stability of sealing system. It is calculated using

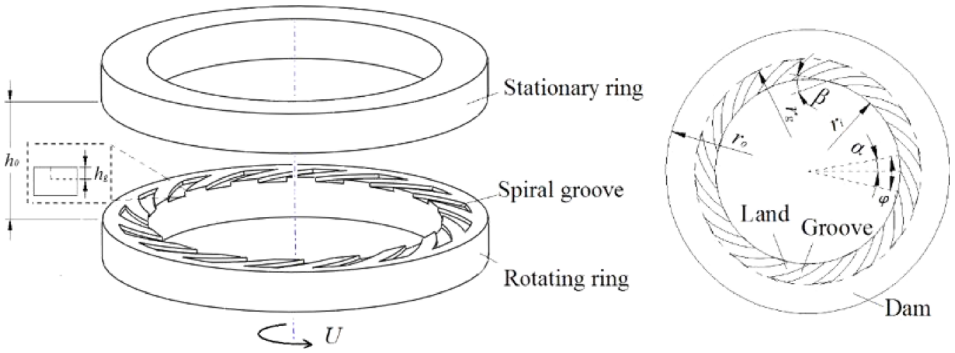

Fig. 1 Schematic diagram of physical model

perturbation method [25] in this study based on the unsteady-state Reynolds equation

$$\frac{\partial}{\partial r}\left(\frac{prh^3}{\mu}\frac{\partial p}{\partial r}\right)+\frac{1}{r}\frac{\partial}{\partial\theta}\left(\frac{ph^3}{\mu}\frac{\partial p}{\partial\theta}\right)=6Ur\frac{\partial(ph)}{\partial\theta}+12r\frac{\partial(ph)}{\partial t} \quad (11)$$

where h is the transient gas film thickness and p is the transient gas film pressure. The seal is perturbed by a small motion $z(t)=z_\varepsilon e^{\lambda+ift}$ in axial, where z_ε is the initial perturbation; λ is the perturbation amplitude; f is the perturbation frequency; and h and p can be expressed, respectively, by

$$h=h_s+z(t) \quad (12)$$

$$p=p_s+p_z z(t)+p_z' z'(t) \quad (13)$$

where h_s is the steady film thickness at the equilibrium position; p_s is the steady film pressure; and p_z and p_z' are the first- and second-order pressure fields, respectively. Considering the state of critical instability where $\lambda=0$, the perturbation Reynolds equation is obtained through substituting Eqs. (12) and (13) into Eq.(11), neglecting higher-order terms, and seeking partial derivative for $z(t)$. Then, the perturbation equation set is obtained according to the characters of real part and imaginary part for plurals. The steady-state Reynolds equation and the perturbation equations set are expressed as

$$\frac{\partial}{\partial r}\left(\frac{p_s rh_s^3}{\mu}\frac{\partial p_s}{\partial r}\right)+\frac{1}{r}\frac{\partial}{\partial\theta}\left(\frac{p_s h_s^3}{\mu}\frac{\partial p_s}{\partial\theta}\right)=6Ur\frac{\partial p_s h_s}{\partial\theta} \quad (14)$$

$$\begin{cases}\dfrac{\partial}{\partial r}\left(\dfrac{3p_s h_s^2 r}{\mu}\dfrac{\partial p_s}{\partial r}\right)+\dfrac{rh_s^3}{\mu}\dfrac{\partial p_s p_{zr}}{\partial r})+\dfrac{1}{r}\dfrac{\partial}{\partial\theta}\left(\dfrac{3p_s h_s^2}{\mu}\dfrac{\partial p_s}{\partial\theta}+\dfrac{h_s^3}{\mu}\dfrac{\partial p_s p_{zr}}{\partial\theta}\right)\\ =6Ur\left(\dfrac{\partial p_s p_{zr}}{\partial\theta}+\dfrac{\partial p_s}{\partial\theta}\right)-12fp_{zi}h_s\\ \dfrac{\partial}{\partial r}\left(\dfrac{rh_s^3}{\mu}\dfrac{\partial p_s p_{zi}}{\partial r}\right)+\dfrac{1}{r}\dfrac{\partial}{\partial\theta}\left(\dfrac{h_s^3}{\mu}\dfrac{\partial p_s p_{zi}}{\partial\theta}\right)\\ =6Ur\dfrac{\partial p_s p_{zi}}{\partial\theta}+12fr(p_{zr}h_s+p_s)\end{cases} \quad (15)$$

where p_{zr} and p_{zi} are the real part and the imaginary part of p_z, respectively. The boundary conditions of perturbation equations set are expressed as

$$\begin{cases}p_{zj}=0, & j=r,i\\ p_{zj}(\theta+2\pi)=p_{zj}(\theta), & j=r,i\end{cases} \quad (16)$$

The axial gas film stiffness is defined as

$$K=-\int_0^{2\pi}\int_{r_i}^{r_o}p_{zr}rdrd\theta \quad (17)$$

All of the above equations are nondimensionalized in order to eliminate the influence of units. The dimensionless terms and the dimensionless performance parameters are defined as

$$\overline{R}=\frac{r}{r_i},\quad \overline{H}=\frac{h}{h_0},\quad \overline{P}=\frac{p}{p_a},\quad \overline{P}_{zr}=\frac{p_{zr}h_0}{p_a},\quad \overline{P}_{zi}=\frac{p_{zi}h_0}{p_a},\quad \Gamma=\frac{f}{U},$$
$$\overline{W}=\frac{W}{p_a r_i^2},\quad \mathrm{COF}=\mathrm{COF},\quad \overline{Q}=\frac{12Q\mu\gamma}{p_a^2h_0^3},\quad \overline{K}=\frac{Kh_0}{p_a r_i^2} \quad (18)$$

The compressibility number is expressed as $\Lambda=(6\mu U/p_a)(r_i/h_0)^2$. The dimensionless Reynolds equation, dimensionless film thickness, and dimensionless boundary condition are expressed as

$$1\overline{R}\frac{\partial}{\partial\overline{R}}\left(\overline{R}\overline{P}\overline{H}\frac{\partial\overline{P}}{\partial\overline{R}}\right)+\frac{1}{\overline{R}^2}\frac{\partial}{\partial\theta}\left(\overline{P}\overline{H}^3\frac{\partial\overline{P}}{\partial\theta}\right)=\Lambda\frac{\partial(\overline{P}\overline{H})}{\partial\theta} \quad (19)$$

$$H(R,\theta)=\begin{cases}1+\dfrac{h_g}{h_0} & (R,\theta)\in\text{groove region}\\ 1 & (R,\theta)\notin\text{groove region}\end{cases} \quad (20)$$

$$\begin{cases}\overline{P}(\overline{R}=1,\theta)=p_i/p_a\\ \overline{P}(\overline{R}=r_o/r_i,\theta)=p_o/p_a\\ \overline{P}(\overline{R}_i,\theta=0)=\overline{P}(\overline{R}_i,\theta=2\pi)\\ \dfrac{\partial\overline{P}}{\partial\theta}(\overline{R}_i,\theta=0)=\dfrac{\partial\overline{P}}{\partial\theta}(\overline{R}_i,\theta=2\pi)\end{cases} \quad (21)$$

The successive over relaxation method is utilized to solve the dimensionless Reynolds equations, and dimensionless pressure are obtained. The dimensionless performance parameters are obtained according to Eq. (18).

2.3 Model of Multi-Objective Optimization. The objective functions of multi-objective optimization problem (MOP) and the constraints of the independent variables are expressed as

$$\begin{aligned}&\min f=[f_1(x),f_2(x),\ldots f_m(x)]\\ &\text{subject to } x \text{ meets certain constraints}\end{aligned} \quad (22)$$

where $f_1(x), f_2(x),\ldots f_m(x)$ are the objective functions in MOP, and x is a vector formed by some independent variables. For a MOP, usually there is not a single optimal solution, but rather a set which is called as Pareto-optimal set. The element in Pareto-optimal set is called Pareto-optimal solution which refers to an acceptable solution, and its meaning is that it is impossible to make one of the objectives better without destroying any other

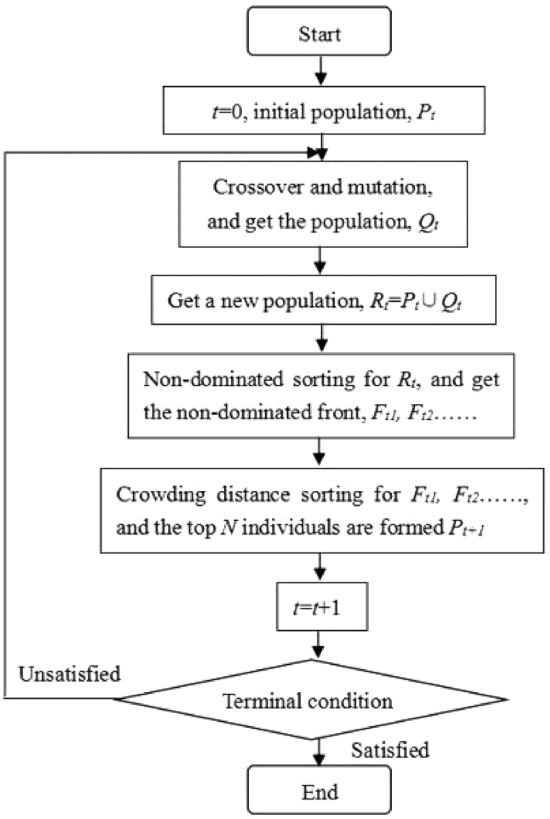

Fig. 2 Flowchart of the NSGA-II

objectives. The distribution of solutions is uniform for an excellent algorithm [26].

The MOP is solved using the elitist nondominated sorting genetic algorithm (NSGA-II), which is the improvement of nondominated sorting genetic algorithm. It brings forward a new fast nondominate sorting approach and its computational complexity is reduced greatly. Figure 2 presents a flowchart of NSGA-II for the MOP [27]. The initial population P_t is generated randomly where $t = 0$, then the population Q_t is obtained through crossover and mutation. The latest population R_t is also obtained which is equal to the union of P_t and Q_t. Then, the nondominated front F_{t1}, F_{t2},…… is obtained through nondominated sorting for R_t. P_{t+1} is formed by top N individuals of the set after crowding distance sorting for F_{t1}, F_{t2},……., then $t = t + 1$. The terminal condition in the present algorithm is that the population distance of the adjacent iterations is less than 1×10^{-5} or the maximum iterations number is more than 200. If the terminal condition is satisfied, algorithm ends, or the algorithm repeats the preceding works and enters the next iteration.

3 Results and Discussion

The effectiveness of the multi-objective optimization approach is checked by a sample application. The values of geometric parameters of the physical model and condition parameters used in this sample are presented in Table 1.

3.1 Single Objective Analyses. In order to determine the important parameters of spiral grooves and the main performance parameters in the multi-objective optimization, the effects of groove-dam ratio, groove-land ratio, spiral angle, and ratio of groove depth and film thickness on the dimensionless performance parameters including gas film lift, leakage rate, COF, and axial gas film stiffness are analyzed, respectively, under the rotational speed of 10,000 rpm (angular velocity of 1047 rad/s). The other parameters are kept constant while analyzing one parameter.

3.1.1 Groove-Dam Ratio. Figure 3 shows the effects of groove-dam ratio δ on the dimensionless performance parameters including gas film lift $\overline{W}$, leakage rate $\overline{Q}$, COF, and axial gas film stiffness $\overline{K}$ at $\kappa = 0.55$, $\beta = \pi/6$, and $\chi = 1$. As shown in this figure, the dimensionless leakage rate is increased when the dimensionless gas film lift and the axial gas film stiffness are improved in most cases, while the dimensionless leakage rate has been dropped when $0.52 \leq \delta \leq 0.74$ where the dimensionless gas film lift is still increasing, and the best value of $\delta = 0.74$ can be judged only in this range. It is difficult to conclude a best value of δ for a larger dimensionless gas film lift and lower dimensionless leakage rate when $\delta < 0.52$ or $\delta > 0.74$. The dimensionless gas film lift and the axial gas film stiffness generally show similar trends as the groove-dam ratio increases: they first increase and reach the maximum value around the groove-dam ratio of 0.74 and 0.82, respectively, and then decrease rapidly. The COF is affected by groove-dam ratio, though the value is extremely small, about 5×10^{-5}–4×10^{-4}. The values of these dimensionless performance parameters change widely with the changing of groove-dam ratio. For example, the range of load carrying capacity is about 110–210. This means that dimensionless performance parameters are influenced significantly by the groove-dam ratio.

3.1.2 Groove-Land Ratio. Figure 4 shows the effects of groove-land ratio κ on dimensionless performance parameters $\overline{W}$, $\overline{Q}$, COF, and $\overline{K}$ at $\delta = 0.45$, $\beta = \pi/6$, and $\chi = 1$. As shown in this figure, the dimensionless leakage rate is increased when the dimensionless gas film lift is improved, as well, the dimensionless gas film lift decreases when the dimensionless leakage rate decreases. The dimensionless gas film lift and the axial gas film stiffness both first increase and reach the maximum value around the groove-land ratio of 0.5, and then decrease as the groove-land ratio increases. Though the COF first increases and then decreases, their values are still extremely small. Similar to the groove-dam ratio, all of the dimensionless performance parameters have a wide range of values in the studied range of groove-land ratio and they are affected by the groove-land ratio greatly.

3.1.3 Spiral Angle. Figure 5 shows the effects of spiral angle β on dimensionless performance parameters $\overline{W}$, $\overline{Q}$, COF, and $\overline{K}$ at $\delta = 0.45$, $\kappa = 0.55$, and $\chi = 1$. As shown in this figure, the dimensionless leakage rate and gas film lift have a similar trend as the spiral angle increases. The dimensionless gas film lift and the axial gas film stiffness both first increase and then decrease slightly as the spiral angle increases, and they reach the maximum value at the spiral angles of 0.7 and 0.87, respectively. The COF always increases with the increasing spiral angle, but its values are only about 1×10^{-4}–4×10^{-4}. All of the dimensionless performance parameters have a wide range in the studied range of the spiral angle.

3.1.4 Ratio of Groove Depth and Film Thickness. Figure 6 shows the effects of the ratio of groove depth and film thickness χ on dimensionless performance parameters $\overline{W}$, $\overline{Q}$, COF, and $\overline{K}$ at $\delta = 0.45$, $\kappa = 0.55$, and $\beta = \pi/6$. As shown in this figure, the dimensionless gas film lift and leakage rate both increase approximately linearly as the ratio of groove depth and film thickness increases. The dimensionless gas film lift is improved by spiral grooves, but the dimensionless leakage rate is also enlarged. The COF with small values of 1×10^{-4}–4×10^{-4} always increases with the increasing ratio of groove depth and film

Table 1 Geometric parameters of the model and condition parameters

Items	Values	
	Single objective	MOP
The inner radius of rotating ring, r_i (mm)	17.9	17.9
The outer radius of rotating ring r_o (mm)	23.4	23.4
Sealed gas dynamic viscosity, μ (MPa·s)	18.448×10^{-12}	18.448×10^{-12}
The pressure at inner radius (MPa)	0.202	0.202
The pressure at outer radius (MPa)	0.101	0.101
Angular velocity, U (rad/s) (rotating speed (rpm))	1047 (10,000)	1047(10,000)
Groove-dam ratio, δ	0.09, 0.27, 0.45, 0.63, 0.81, 1	0–1
Spiral angle, β (rad)	0.17, 0.35, 0.52, 0.7, 0.87, 1.05, 1.22, 1.39	0–$\pi/2$
Groove-land ratio, κ	0.09, 0.27, 0.45, 0.63, 0.81, 1	0–1
Spiral groove number, n	16	16
Ratio of groove depth and film thickness, χ	0.4, 0.6, 0.8, 1, 1.2, 1.4	0.4–2
Gap of two specimen, h_0 (μm)	10	10
Dimensionless perturbation frequency, Γ	1	1
Compressibility number, Λ	35.114	35.114

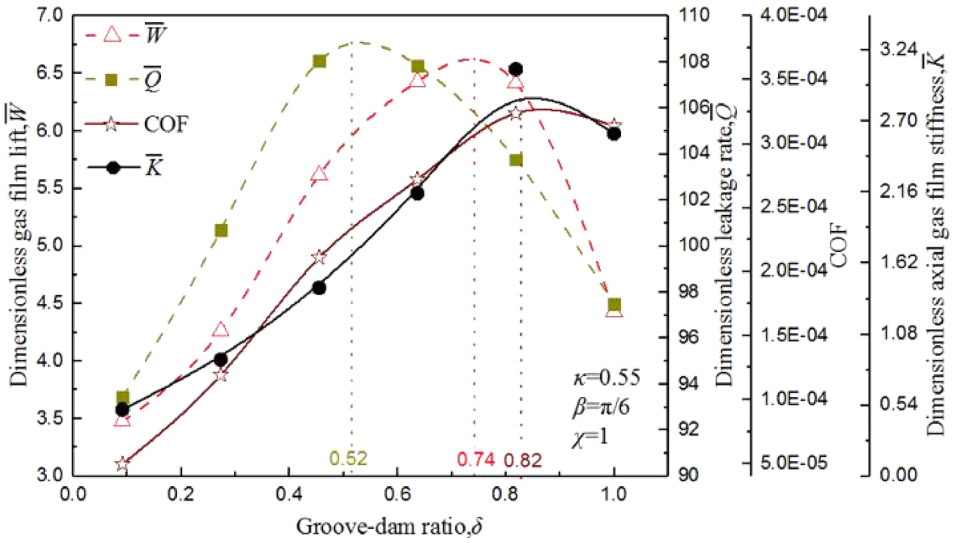

Fig. 3 Effects of groove-dam ratio δ on the four dimensionless performance parameters at $\kappa = 0.55$, $\beta = \pi/6$, and $\chi = 1$

thickness. The dimensionless performance parameters are affected greatly by the ratio of groove depth and film thickness.

In order to verify that the above results are not occasional, more values of these parameters of spiral grooves are calculated. Figure 7 shows the dimensionless performances parameters distribution clouds with the variation of different geometric parameters. It can be seen that the results did not change in general, which means that the variations of these dimensionless performance parameters with the changing of spiral groove parameters are universal. It is reasonable to determine the critical dimensionless performance parameters and variables in multi-objective optimization through the above analysis.

According to the above analysis it is known that: (a) the dimensionless leakage rate often increases when the dimensionless gas film lift and the axial gas film stiffness are improved by spiral grooves, it is difficult to obtain the optimal parameters of spiral grooves due to the conflict of leakage property and load carrying characteristic, which illustrates the necessity of multi-objective optimization. (b) The dimensionless gas film lift and the axial gas film stiffness often change similarly with the changing of spiral groove parameters, and they are both the indices to evaluate the load carrying characteristic. So, one of them is enough for the parameters optimization of spiral grooves, the dimensionless gas film lift is selected in the following study. (c) The COF can be seen as a factor that does not need special attention, because it is extremely small. (d) The parameters of spiral grooves, including groove-dam ratio, groove-land ratio, spiral angle, and ratio of groove depth and film thickness, have significant effects on the performance parameters, so all of them are selected as independent variables in the following study.

3.2 Multi-Objective Optimization. The model of multi-objective optimization in this study is expressed by

$$\begin{aligned} &\min\ f(x) = \left[-\overline{W}(x), \overline{Q}(x)\right], x = [\delta, \kappa, \beta, \chi] \\ &\text{subject to}\ \ \delta \in (0,1), \kappa \in (0,1), \beta \in \left(0, \frac{\pi}{2}\right), \chi \in [0.4, 1.4] \end{aligned} \tag{23}$$

where x is a vector formed by the spiral groove parameters and the constraints of x are shown in Eq. (19). The dimensionless gas film lift and leakage rate are functions of x, and the expressions

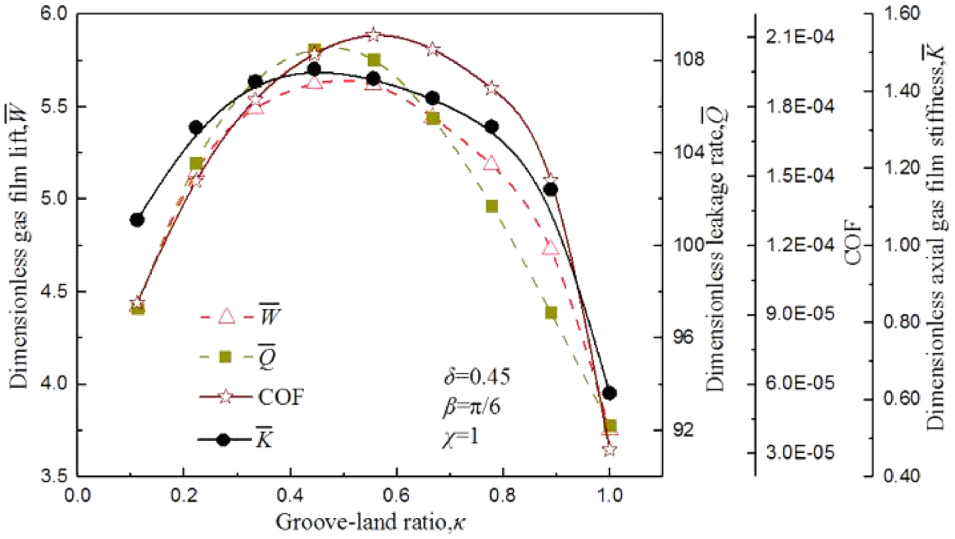

Fig. 4 Effects of groove-land ratio κ on the four dimensionless performance parameters at $\delta = 0.45$, $\beta = \pi/6$, and $\chi = 1$

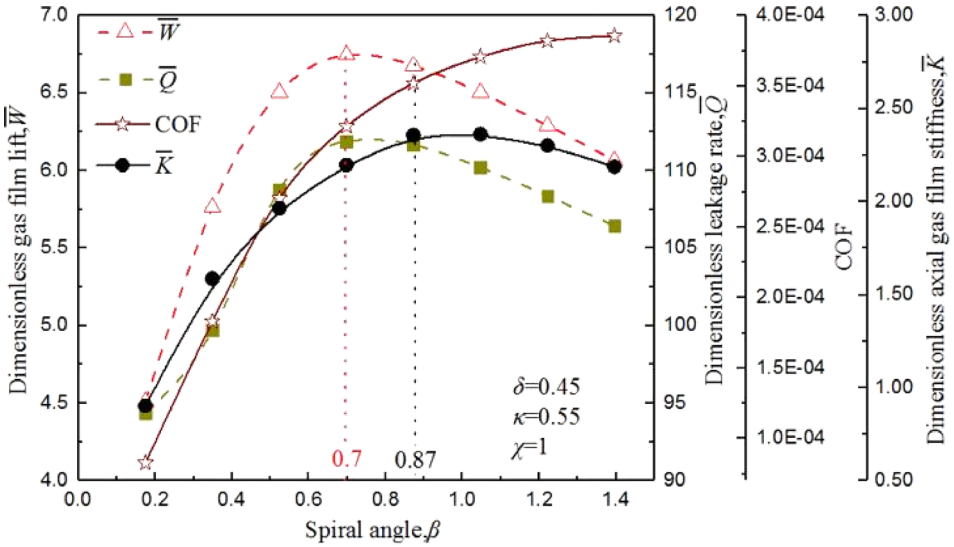

Fig. 5 Effects of spiral angle β on the four dimensionless performance parameters at $\delta = 0.45$, $\kappa = 0.55$, and $\chi = 1$

are $\overline{W}(x)$ and $\overline{Q}(x)$, respectively. Because the minimum values of objective functions are the goal of this MOP, $-\overline{W}(x)$ is taken as an objective function according to the practical meaning of $\overline{W}(x)$. The MOP is solved using NSGA-II according to the flowchart in Fig. 2. The Pareto-optimal set and optimal objectives are obtained, respectively. The number of solutions in Pareto-optimal set is equal to the product of population size and Pareto fraction. Too many solutions are unnecessary because they are continuous and the neighboring solutions have very high similarities. So population size is set to 200 and Pareto fraction is set to 4.5%, i.e., the number of solutions is 9, in order to show the optimal shapes clearly. The shapes of spiral grooves are drawn according to the optimal parameters. The Pareto-optimal set and the shapes of spiral grooves are presented in Table 2 and Fig. 8.

As can be seen from Table 2 and Fig. 8, the optimal groove-dam ratio, groove-land ratio, and ratio of groove depth and film thickness increase approximately from solution 1 to solution 9. However, spiral angles in the Pareto-optimal set are almost unchanged. It means that the spiral angle may be taken a constant in the parameters optimization, which can reduce the complexity and improve the computational efficiency of the multi-objective optimization. This problem will be solved by collinearity diagnostics in Sec. 3.3.

Figure 9 shows the results of multi-objective optimization. The horizontal axis shows the optimal dimensionless leakage rate and the vertical axis shows the optimal dimensionless gas film lift. The points in this figure are the optimal solutions of objectives corresponding to the optimal parameters in Table 2, which divide the area into two parts. For all of spiral groove parameters except optimal parameters, their dimensionless gas film lift and leakage rate will fall in the shaded area according to the principle of multi-objective optimization. The meaning of solutions is that it is impossible to make one objective better if the other objective is not deteriorated. In other words, the solutions can provide an optimal value of one objective when the value of the other objective is fixed. For example, solution 5 can provide the largest dimensionless gas film lift than other grooves for the dimensionless leakage rate of 107.5; in other words, other grooves cannot provide the dimensionless gas film lift as high as 7.8 for this dimensionless leakage rate. Similarly, solution 5 can provide the lowest

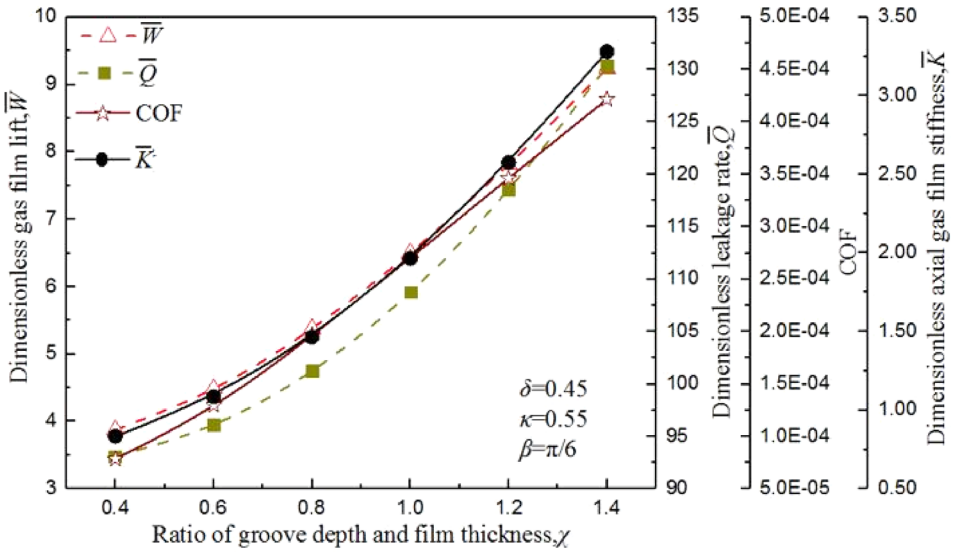

Fig. 6 Effects of ratio of groove depth and film thickness χ on the four dimensionless performance parameters at $\delta = 0.45$, $\kappa = 0.55$, and $\beta = \pi/6$

dimensionless leakage rate than other grooves under the dimensionless gas film lift of 7.8.

It can also be observed from Fig. 9 that there is a considerable span for the values of optimal objectives. That is, the optimization results can provide a reference for a variety of leakage requirements. For example, parameters of solution 5 can be selected to design the spiral grooves on mechanical seals if the dimensionless leakage rate of not more than 107.5 is allowed for a certain

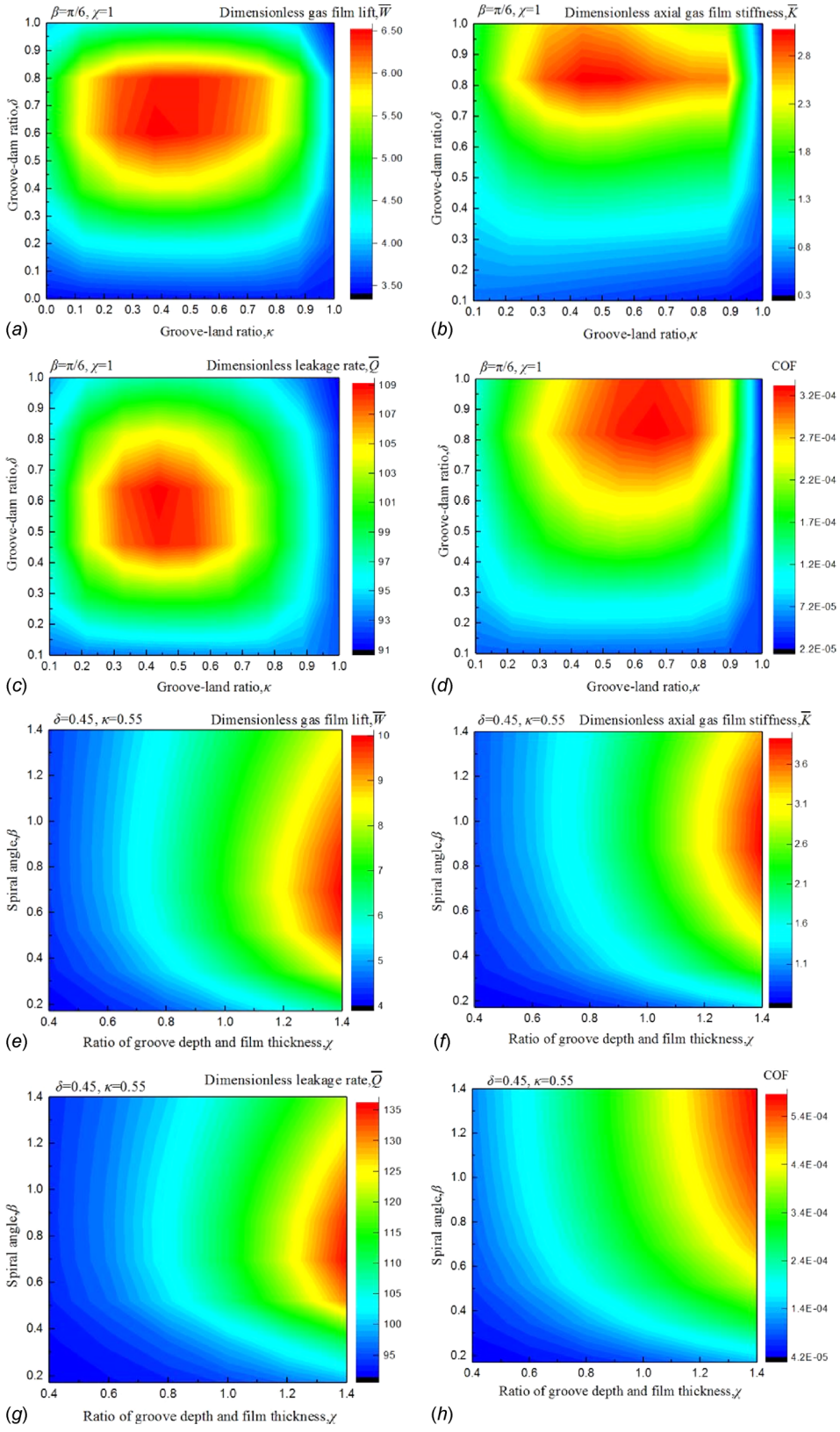

Fig. 7 Distribution clouds for different parameters: (*a*) $\overline{W}$ distribution with κ and δ, (*b*) $\overline{K}$ distribution with κ and δ, (*c*) $\overline{Q}$ distribution with κ and δ, (*d*) COF distribution with κ and δ, (*e*) $\overline{W}$ distribution with β and χ, (*f*) $\overline{K}$ distribution with β and χ, (*g*) $\overline{Q}$ distribution with β and χ, and (*h*) COF distribution with β and χ

Table 2 Pareto-optimal set

Solutions	1	2	3	4	5	6	7	8	9
δ	0.52	0.70	0.63	0.71	0.67	0.70	0.67	0.71	0.72
κ	0.06	0.22	0.42	0.62	0.60	0.67	0.56	0.60	0.71
β	1.27	1.24	1.22	1.20	1.22	1.21	1.20	1.20	1.21
χ	0.50	0.87	1.04	1.30	1.46	1.61	1.67	1.80	2.00

working condition. In this way, the spiral grooves can meet the requirement of the dimensionless leakage rate and can generate the dimensionless gas film lift as large as possible at the same time.

Moreover, as shown in Fig. 9, the growth rate of optimal dimensionless gas film lift is getting smaller and smaller as the optimal dimensionless leakage rate increases linearly. It means that when the dimensionless gas film lift increases slightly, the dimensionless leakage rate will increase sharply. In other words, blindly pursuing the maximum gas film lift is not appropriate in the design of spiral grooves on mechanical seals because the drastic rises may occur in the leakage rate.

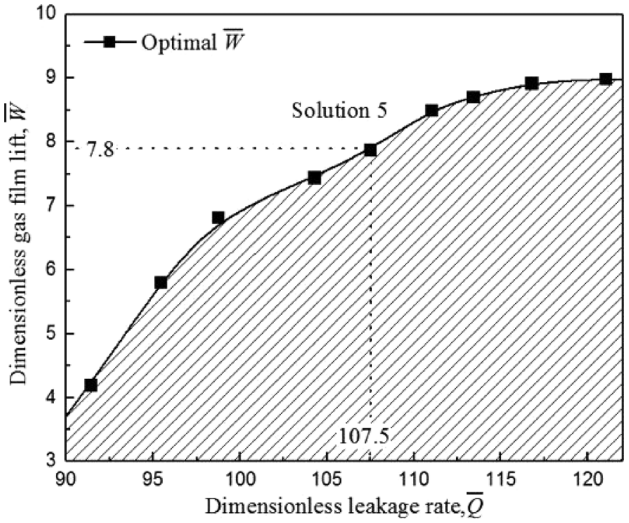

Fig. 9 Results of multi-objective optimization

3.3 Collinearity Diagnostics. In order to analyze the importance of different parameters in the optimization results, collinearity diagnostics is utilized to find the less important factors. Then, the variables are taken as constants in the Pareto-optimal set. Finally, the objective values are recalculated to study the influence of collinearity diagnostics on the optimization results.

All of the data are standardized. The standardization formula is expressed as

$$\overline{s}_i = \frac{s_i - \text{mean}(s)}{\sigma(s)} \tag{24}$$

where s is a symbol that represents the set of each parameter' values, s_i is the element in s, $\overline{s}_i$ is the standardized value of s_i, mean(s) is the average value of set s, and $\sigma(s)$ is the root-mean-square of set s.

Table 3 is the collinearity diagnostics result. According to the principle of collinearity diagnostics, it is generally accepted that there is a collinearity between these variables if their variance proportions are close to 1 in the same row. Based on this principle, it is determined that the spiral angle and the constant are collinear. In fact, the value of spiral angle can take a constant of 1.22 that the mean of optimal values in Pareto-optimal set.

The set is called simplified optimal set that spiral angles are taken as 1.22 and other parameters are taken the values in Pareto-optimal set. The objectives under the parameters in simplified optimal set are calculated, and the errors of objectives caused by fixing the spiral angle are calculated according to the following formula:

$$\text{error} = \frac{S_2 - S_1}{S_1} \times 100\% \tag{25}$$

where S_1 and S_2 are symbols that represent the objectives values in Pareto-optimal set and simplified optimal set, respectively.

The errors and objectives' values under these two sets are shown in Fig. 10. It can be observed that the optimal dimensionless gas film lift of simplified optimal set is slightly smaller than that of Pareto-optimal set, and the optimal dimensionless leakage rate of simplified optimal set is slightly larger than that of Pareto-optimal set. It is reasonable that the objectives become worse slightly due to the fixing of one independent variable. It also can be observed in Fig. 10 that the effect of fixing the spiral angle on the optimal dimensionless gas film lift is most obvious, and the maximum error is only −0.7%. In fact, all of the errors are quite small. In other words, fixing the spiral angle has little influence on the optimization results, which confirms the feasibility of removing the less important factor in multi-objective optimization by collinearity diagnostics. This method can simplify the design of

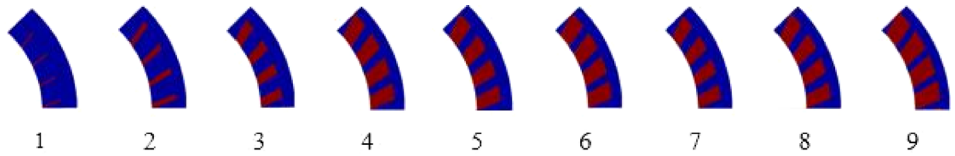

Fig. 8 Optimal shapes of spiral grooves

Table 3 Collinearity diagnostics results

			Variance proportions				
Dimension	Eigen values	Condition index	Constant	δ	κ	β	χ
1	4.848	1.000	0.00	0.00	0.00	0.00	0.00
2	0.140	5.876	0.00	0.00	0.04	0.00	0.02
3	0.009	22.802	0.00	0.00	0.57	0.00	0.97
4	0.002	44.950	0.00	0.82	0.09	0.00	0.01
5	2.243×10^{-5}	464.901	1.00	0.18	0.30	1.00	0.00

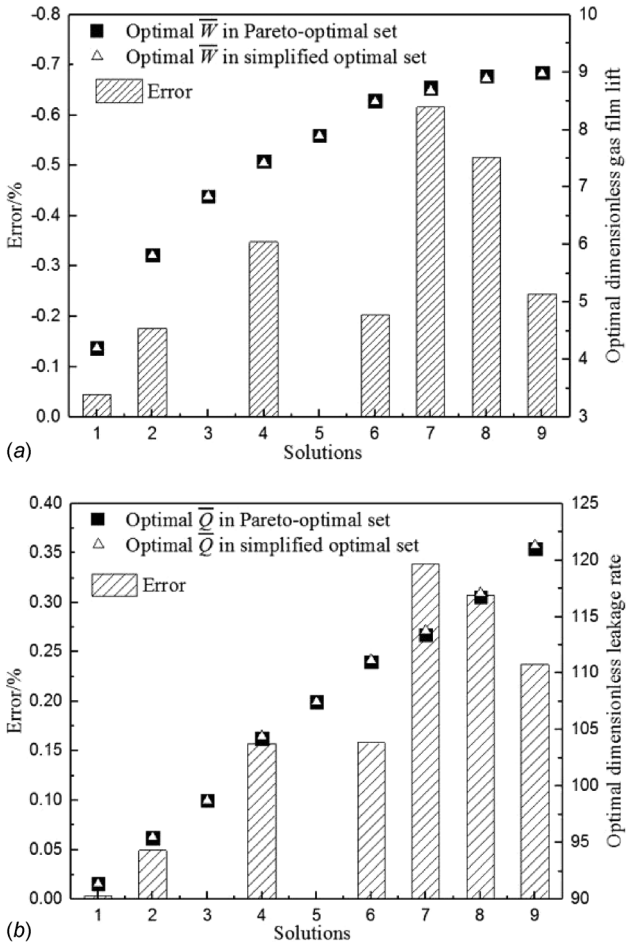

Fig. 10 Errors of objectives in simplified optimal set compared with Pareto-optimal set: (*a*) optimal dimensionless gas film lift and (*b*) optimal dimensionless leakage rate

spiral grooves on mechanical seals and provide guidance for the multi-objective optimization of surface textures on mechanical seals under other working conditions.

4 Conclusions

In this study, a multi-objective optimization approach is presented due to the conflict of leakage property and load carrying characteristic. Spiral grooves are optimized under a specific condition to verify the effectiveness of this method. The objectives including dimensionless gas film lift and dimensionless leakage rate and independent variables including spiral angle, groove-dam ratio, groove-land ratio, and ratio of groove depth and film thickness in the multi-objective optimization are determined by single objective analysis.

A Pareto-optimal set is obtained based on NSGA-II, and each solution in this set can get the highest dimensionless gas film lift under a specific requirement of the dimensionless leakage rate. The wide span of solutions can provide a reference for a variety of leakage requirements. Furthermore, the spiral angle can be taken as a constant for the simplicities of grooves design and optimization algorithm by collinearity diagnostics.

The specific sample shows the effectiveness of the multi-objective optimization approach, and the other working conditions can also be analyzed using the method when the actual condition parameters are specified.

Funding Data

- Jiangsu Innovation Program for Graduate Education (Grant No. KYLX16_0326).
- National Natural Science Foundation of China (Grant No. 51675268).
- Fundamental Research Funds for the Central Universities (Grant No. NZ2016106).
- Natural Science Research Fund of Higher Education of Anhui Province (Grant No. KJ2016A093).

Nomenclature

e = natural constant
f = perturbation frequency, s^{-1}
F_t = nondominated front
h = gas film thickness/transient gas film thickness, μm
h_g = groove depth, μm
h_s = film thickness at equilibrium position, μm
h_0 = sealing clearance, μm
$\overline{K}$ = dimensionless axial gas film stiffness
M = average molecular mass of gas, g/mol
n = groove number
p = gas film pressure/transient gas film pressure, MPa
p_a = atmospheric pressure, MPa
p_i = pressure at inner radius, MPa
p_o = pressure at outer radius, MPa
p_s = steady film pressure, MPa
p_z = first-order pressure field
p_{zi} = imaginary part of p_z
p_{zr} = real part of p_z
P_t = population at N_{th} iteration
P_0 = initial population
$\overline{Q}$ = dimensionless leakage rate
Q_t = population obtained by crossover and mutation
r = coordinate in radial direction
R = proportional constant of ideal gas
r_g = outer radius of sealing ring, mm
r_i = inner radius of sealing ring, mm
r_o = outer radius of sealing ring, mm
R_t = union of R_t and Q_t
s = symbol represents a set of parameters
s_i = element in s
$\overline{s}_i$ = the standardized value of s_i
S_1 = symbol represents the objective values in Pareto-optimal set
S_2 = symbol represents the objective values in simplified optimal set
T = absolute temperature, K
U = angular velocity, rad/s
$\overline{W}$ = dimensionless gas film lift
z_ε = initial perturbation
α = angle corresponding to groove
β = spiral angle
γ = the gas pressure to density ratio
Γ = dimensionless perturbation frequency
δ = groove-dam ratio
θ = coordinate in circumferential direction
κ = groove-land ratio
λ = perturbation amplitude
Λ = compressibility number
μ = dynamic viscosity of gas, MPa·s
ρ = gas density, g/cm^3
φ = angle corresponding to land and groove
χ = ratio of groove depth and film thickness

References

[1] Etsion, I., Kligerman, Y., and Halperin, G., 1999, "Analytical and Experimental Investigation of Laser-Textured Mechanical Seal Faces," Tribol. Trans., **42**(3), pp. 511–516.
[2] Yu, H., Deng, H., Huang, W., and Wang, X., 2011, "The Effect of Dimple Shapes on Friction of Parallel Surfaces," Proc. Inst. Mech. Eng., Part J, **225**(8), pp. 693–703.
[3] Shen, C., and Khonsari, M. M., 2013, "Effect of Dimple's Internal Structure on Hydrodynamic Lubrication," Tribol. Lett., **52**(3), pp. 415–430.
[4] Ma, C., Bai, S., Peng, X., and Meng, Y., 2013, "Improving Hydrophobicity of Laser Textured Sic Surface With Micro-Square Convexes," Appl. Surf. Sci., **266**, pp. 51–56.

[5] Yu, H., Huang, W., and Wang, X., 2013, "Dimple Patterns Design for Different Circumstances," Lubr. Sci., **25**(2), pp. 67–78.
[6] Zhang, B., Huang, W., Wang, J., and Wang, X., 2013, "Comparison of the Effects of Surface Texture on the Surfaces of Steel and UHMWPE," Tribol. Int., **65**, pp. 138–145.
[7] Wang, X., Adachi, K., Otsuka, K., and Kato, K., 2006, "Optimization of the Surface Texture for Silicon Carbide Sliding in Water," Appl. Surf. Sci., **253**(3), pp. 1282–1286.
[8] Wang, T., Huang, W., Liu, X., Li, Y., and Wang, Y., 2014, "Experimental Study of Two-Phase Mechanical Face Seals With Laser Surface Texturing," Tribol. Int., **72**, pp. 90–97.
[9] Feldman, Y., Kligerman, Y., Etsion, I., and Haber, S., 2005, "The Validity of the Reynolds Equation in Modeling Hydrostatic Effects in Gas Lubricated Textured Parallel Surfaces," ASME J. Tribol., **128**(2), pp. 345–350.
[10] Qiu, Y., and Khonsari, M. M., 2011, "Performance Analysis of Full-Film Textured Surfaces With Consideration of Roughness Effects," ASME J. Tribol., **133**(2), p. 021704.
[11] So, H., and Chen, C., 2004, "Effects of Micro-Wedges Formed Between Parallel Surfaces on Mixed Lubrication—Part I: Experimental Evidence," Tribol. Lett., **17**(3), pp. 513–520.
[12] Lee, S. C., and Zheng, X., 2013, "Analyses of Both Steady Behavior and Dynamic Tracking of Non-Contacting Spiral-Grooved Gas Face Seals," Comput. Fluids, **88**, pp. 326–333.
[13] Wan, Y., and Xiong, D., 2008, "The Effect of Laser Surface Texturing on Frictional Performance of Face Seal," J. Mater. Process. Technol., **197**(1–3), pp. 96–100.
[14] Mcnickle, A. D., and Etsion, I., 2004, "Near-Contact Laser Surface Textured Dry Gas Seals," ASME J. Tribol., **126**(4), pp. 788–794.
[15] Shi, L., Wang, X., Su, X., Huang, W., and Wang, X., 2015, "Comparison of the Load-Carrying Performance of Mechanical Gas Seals Textured With Microgrooves and Microdimples," ASME J. Tribol., **138**(2), p. 021701.
[16] Razzaque, M. M., and Faisal, M. T. R., 2007, "Performance of Mechanical Face Seals With Surface Micropores," J. Mech. Eng., **37**, pp. 77–80.
[17] Salant, R. F., and Homiller, S. J., 1992, "The Effects of Shallow Groove Patterns on Mechanical Seal Leakage," Tribol. Trans., **35**(1), pp. 142–148.
[18] Xiao, K., Huang, W., Gao, W., Liu, X., and Wang, Y., 2016, "A Semi-Analytical Model of Spiral-Groove Face Seals: Correction and Extension," Tribol. Trans., **59**(6), pp. 971–982.
[19] Qiu, Y., and Khonsari, M. M., 2012, "Thermohydrodynamic Analysis of Spiral Groove Mechanical Face Seal for Liquid Applications," ASME J. Tribol., **134**(2), p. 021703.
[20] Wang, B., and Zhang, H., 2011, "Numerical Analysis of a Spiral-Groove Dry-Gas Seal Considering Micro-Scale Effects," Chin. J. Mech. Eng., **24**(1), pp. 146–153.
[21] Faria, M. T. C., 2001, "An Efficient Finite Element Procedure for Analysis of High-Speed Spiral Groove Gas Face Seals," ASME J. Tribol., **123**(1), pp. 205–210.
[22] Zirkelback, N., 2000, "Parametric Study of Spiral Groove Gas Face Seals," Tribol. Trans., **43**(2), pp. 337–343.
[23] Zhou, J., Gu, B., and Chen, Y., 2007, "An Improved Design of Spiral Groove Mechanical Seal," Chin. J. Chem. Eng., **15**(4), pp. 499–506.
[24] Liu, Z., Liu, Y., and Liu, X., 2007, "Optimization Design of Main Parameters for Double Spiral Grooves Face Seal," Sci. China Ser. E, **50**(4), pp. 448–453.
[25] Zirkelback, N., and Andreś, L. S., 1999, "Effect of Frequency Excitation on Force Coefficients of Spiral Groove Gas Seals," ASME J. Tribol., **121**(4), pp. 853–861.
[26] Li, H., and Zhang, Q., 2009, "Multiobjective Optimization Problems With Complicated Pareto Sets, MOEA/D and NSGA-II," IEEE Trans. Evol. Comput., **13**(2), pp. 284–302.
[27] Deb, K., Pratap, A., Agarwal, S., and Meyarivan, T., 2002, "A Fast and Elitist Multiobjective Genetic Algorithm: NSGA-II," IEEE Trans. Evol. Comput., **6**(2), pp. 182–197.